fluids

MDPI

Article

Vortex-Breakdown Efficiency of Planar Regular Grid Structures—Towards the Development of Design Guidelines

Julien Sirois [1,2], Marlène Sanjosé [1,*], Fabian Sanchez [2] and Vladimir Brailovski [1]

[1] Department of Mechanical Engineering, École de Technologie Supérieure, Montréal, QC H3C 1K3, Canada; julien.sirois.1@ens.etsmtl.ca (J.S.); vladimir.brailovski@etsmtl.ca (V.B.)
[2] Siemens Energy Canada Limited, Montréal, QC H8T 3H1, Canada; fabian.sanchez@siemens-energy.com
* Correspondence: marlene.sanjose@etsmtl.ca

Abstract: The work presented here aims to provide design guidelines to create vortex-damping structures. A design of experiment was developed to investigate the individual and combined effects of the geometrical properties of planar regular grid structures, i.e., the wire diameter, the porosity, and the inter-grid spacing, on their vortex-breakdown performance. The simulations were carried out using a commercial unsteady RANS solver. The model relies on the Von Karman street effect to generate vortices in a pipe which are convected downstream, where they interact with an array of grids. The vortex-breakdown efficiency is characterized by the pressure drop, the residual turbulent kinetic energy, the flow homogeneity, and the size of the transmitted vortices. The wire diameter is shown to be an important design lever as it affects the level of distortion of the transmitted vortices. Increasing the number of grids augments the pressure loss, but their contribution to vortex breakdown is otherwise limited when the wire diameter is small. The influence of grid spacing strongly depends on the wire diameter and grid alignment. For instance, minimizing this gap reduces the pressure drop for the inline configurations, but increases the pressure drop for the offset configurations.

Keywords: vortex breakdown; grid interactions; RANS; confined flow; Von Karman street

Citation: Sirois, J.; Sanjosé, M.; Sanchez, F.; Brailovski, V. Vortex-Breakdown Efficiency of Planar Regular Grid Structures—Towards the Development of Design Guidelines. *Fluids* **2024**, *9*, 43. https://doi.org/10.3390/fluids9020043

Academic Editors: Nilanjan Chakraborty and Markus Klein

Received: 21 December 2023
Revised: 2 February 2024
Accepted: 6 February 2024
Published: 8 February 2024

1. Introduction

Industrial gas turbines are a key component in power generation. To maintain their competitiveness, operators strive to reduce their operating cost and manufacturers continuously work to improve the efficiency of their engines. One avenue to improve efficiency is in the optimization of air management in the combustion system by reducing the pressure losses upstream of the combustors.

A particularity of Dry Low Emission (DLE) combustion systems is that the air and fuel are thoroughly mixed upstream of the combustion chamber. This ensures a very clean and uniform combustion, allowing these engines to achieve very low NOx levels. However, it is primordial for the highly turbulent flow field with pronounced non-homogeneity from the successive blade cascade wakes coming from the compressor stage to be conditioned before it can enter the combustion system, as large vortices can lead to the formation of lean air pockets, which are detrimental to combustion uniformity and can result in excessive NOx levels and harmful combustion dynamics [1]. Stochastic structures like metal foams are highly effective at damping vorticity and homogenizing the flow, and have been used successfully for many years. So, why fix it if it's not broken? Because they incur a considerable pressure loss impacting the overall efficiency.

Considering the capabilities of modern additive manufacturing techniques, the idea of developing a substitute lattice structure germinated, with a focus on reducing the pressure loss while retaining the homogenizing power. Confronted with an abundance of lattice types and the scarce literature on their interaction with vortices, the focus quickly shifted to understanding how the geometrical properties of a lattice structure influence their vortex-breakdown performance by studying grids.

The vortex–porous screen interaction has been studied by a few authors in the past, each typically focusing on a single variable at a time. These studies, experimental for the most part, employed various visualization techniques for their measurements. All of the reported studies relied on a piston to create a vortex ring moving through a stationary fluid inside a large tank (water [2–6], air [7,8]). The Reynolds number, based on the piston diameter and exit velocity, ranges between 1000 and 6000 in the reported studies in Table 1.

Table 1. Comparison of the previous studies on the interaction of vortex rings and porous screens.

Author(s)	Method	φ [%]	d_w [mm]	ε [mm]	Re
Hrynuk et al. [2,3]	PLIF, MTV	64	0.18–2.67	Single	2300–4200
Musta and Krueger [4,5]	DPIV	50–84	3.18	25, 50	1000–3000
Naaktgeboren et al. [6]	DPIV, PLIF	44–79	0.71	Single	3000, 6000
An et al. [7,8]	Fog, RANS	30–80	1.00	Single	700–3000
Cheng et al. [9]	LBM	0–100	0.015–0.1 *	Single	500–5000
Present study	IU-RANS	55–85	0.25–1.00	2.5–7.5	3200

* The wire diameter in Cheng et al. [9] is a function of the vortex diameter.

Both qualitative and quantitative techniques were adopted by the investigators to study the behavior of vortices passing through grids. Planar Laser-Induced Luminescence (PLIF) and fog generators were used to visualize the vortex and study how it deforms and reforms. The use of trackers was also employed by some authors (particle image velocimetry (PIV) and molecular tagging velocimetry (MTV)) to measure the variation in the vortex size and the kinetic energy. Both techniques are complimentary. This has also been investigated numerically by some authors [7–9].

Past studies typically focused on a single parameter at one time. Naaktgeboren et al. [6] and An et al. [7,8] focused on the effect of porosity, while Hrynuk et al. [2,3] studied the influence of the grid wire diameter. The effect of placing multiple grids in series was studied by Musta and Krueger [4,5], who also varied the porosity. Finally, Cheng et al. [9] used numerical simulations to study the influence of the porosity, wire size, and grid thickness.

It was observed that the effect of the porosity primarily impacts the radial expansion of the vortex ring and the intensity of the residual kinetic energy. The restriction caused by the lower porosity grids resulted in an interaction similar to a solid wall, with the radial expansion of the vortex ring as it approached the porous screen [6]. When the porosity was large, this radial distortion of the primary vortex was not observed. The transmitted kinetic energy was strongly dependent of the grid porosity, but even very porous grids reduced the turbulent kinetic energy (TKE) transmission by 40–60% [2–6]. The size of the transmitted vortical sub-structures varied substantially with the porosity, with larger openings permitting larger sub-structures to form, but were weakly affected by the inter-grid spacing.

The wire diameter was shown to have the greatest effect on the reformation behavior of the vortex downstream. When the diameter was small (d_w < 0.50 mm), the vortex reformed instantly with minimal distortion of the core. In the intermediate range (0.50 < d_w < 1.60 mm), the vortex core distortion increased with the wire diameter and delayed the reformation of the ring. For larger wires (d_w > 1.60 mm), the transmitted vortex core was too disrupted to be reformed downstream. Notably, small vortical sub-structures formed downstream of the larger wires, consistent with the vortex shedding behind a circular bluff body [2,3].

The effect of placing multiple grids in series was studied by Musta and Krueger [4,5]. The vortex rings systematically collapsed into multiple vortical sub-structures passed the first grid, with no coherent structures beyond the third grid, although the large wire size of the grids employed likely contributed to the vortex breakdown to some extent. The effect of the inter-grid spacing was stronger when the porosity was large. Cheng et al. [9] observed similar trends when increasing the thickness of the grids.

On the influence on the jet Reynolds number, a transition in the vortex regime from laminar to turbulent was observed [6] at around Re = 1000. Beyond that, increasing the Reynolds number essentially scales the kinetic energy and the penetration of the vortex rings. It was also observed that the rate of decay of the transmitted TKE increases with the Re [2–5].

This topic was also investigated numerically by some others, again using a piston to generate a vortex ring. Cheng et al. [9] used the Lattice Boltzmann Method (LBM) to measure the effect of the porosity, wire diameter, and Reynolds number. The results obtained were generally in good agreement with the experimental results obtained by previous authors, including [3,4,6].

More recently, An et al. [7,8] reproduced their experimental tests using a classical unsteady Reynolds-Averaged Navier–Stokes (RANS) solver for incompressible fluid. The authors used the SIMPLEC algorithm for the pressure–velocity coupling and the PRESTO (PREssure STaggering Option) for the pressure interpolation. The results obtained numerically regarding the trajectory of the vortex core and the influence of the Reynolds number were in good agreement with their experimental results. This indicates that IU-RANS can also be a good option to study vortex breakdown.

The work presented here brings forth three novelties. Firstly, the design of experiment (DoE) developed for this investigation covers all the grid parameters, which is essential to understanding their individual and combined effects on vortex breakdown. The knowledge gained is crucial in the context of developing design rules to guide the conception of more efficient geometries.

Secondly, in addition to the residual turbulent kinetic energy and the transmitted vortex size, two new key performance indicators (KPIs) are evaluated: the flow field uniformity and the pressure loss. These KPIs are detailed in Section 2.6.

Lastly, where previous authors used a piston to generate a vortex ring moving through a stationary fluid inside a large tank, this study generates vortices using the Von Kármán street effect by placing a cylindrical bluff body perpendicular to a moving fluid confined inside a pipe. The use of a bluff body to generate coherent vortex structures allows the grids to be tested in the presence of mean flow. At the same time, the vortex sizes and turbulent intensities can be evaluated, as well as the pressure losses and the flow homogenization across the grids. This vortex generation method is a classical approach to flow interaction problems. Cylindrical bluff bodies are frequently used to mimic stage interaction problems in turbomachinery [10,11]. This approach is preferred because it is more representative of the actual flow in a combustor where coherent vortices are convected with the mean flow. In addition, this investigation is carried out using an unsteady RANS solver. The low computational cost of this method is essential to simulate all the configurations in the test matrix.

Section 2 presents the optimization criteria, the methodology, the DoE, and the KPIs. Section 3 presents the results, and a case study is presented in Section 4.

2. Methodology

2.1. Optimization Criteria

In the context of developing a more efficient alternative to metallic foams, the first step is to establish the key performance indicators (KPIs). The first metric is the pressure loss (ΔP), which shall be minimized. A pressure loss leading to the combustor takes away some of the energy which would otherwise be used in the combustion air or for cooling. The second metric is the transmitted turbulent kinetic energy (TKE), i.e., the residual energy downstream of the grids. Depending on the flame type, a turbulent flow may be desirable because it enhances the mixing of the air–fuel mixture, leading to a more uniform combustion. The third KPI is the uniformity of the velocity field, which should be as homogenous as possible. The presence of streak within the flow can cause instability. The final metric is the size of the transmitted vortices. Large vortices are never desirable

because the fuel cannot penetrate inside the vortex, which can result in lean air pockets. This is particularly important with premix systems to avoid auto-ignition.

2.2. Computational Domain

The computational domain and important dimensions are represented in Figure 1. In its baseline configuration, the model simply consists of a Ø50 mm × 450 mm long pipe with the cylindrical bluff body (d = 5 mm), perpendicular to the flow, located 200 mm downstream of the inlet. As the air passes over the bluff body, vortices form and shed periodically, creating a Von Karman alley. The shed vortices are then convected downstream by the flow. For the DoE, grids are introduced 35 mm downstream from the bluff body axis. The domain is reduced by using a symmetry plane along the length of the tube. Eight virtual planes (Figure 1: P_{In}, P_{BB}, P_{Grid}, P_{M1}, P_{M2}, P_{M3}, P_{Out}, and the XY cross plane) are created to monitor the solution. The blockage ratio caused by the bluff body is 0.1, which is relatively small and should not affect the vortex dynamics [12]. This geometry imitates the passage leading to the combustor where the foam is employed and replicates similar confinement effects.

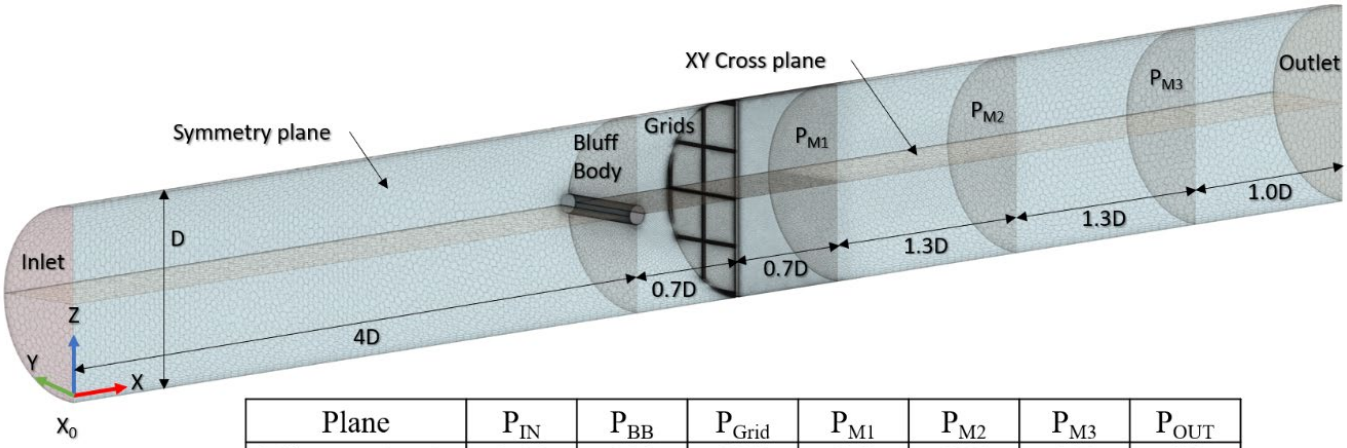

Plane	P_{IN}	P_{BB}	P_{Grid}	P_{M1}	P_{M2}	P_{M3}	P_{OUT}
Distance (mm)	0.00	200	235	270	335	400	450

Figure 1. Computational domain.

The effect of the symmetry plane was verified by comparing two complete models (one inline, one offset) with the half-models reported in this study. The differences in the KPIs between the half and full models are in the order of ±5%. It should be noted that the offset configurations are still roughly symmetrical since the grids are regular, i.e., the wires are not randomly distributed. Overall, the effect of the symmetry plane is acceptable and represents a good trade-off between accuracy and computational costs.

2.3. Numerical Parameters

The unsteady RANS simulations in the present study were performed in Star-CCM+ (v2206) using the Realizable 2-layer K-ε turbulence model [13] and the implicit unsteady solver. Pressure–velocity coupling was achieved using the SIMPLE algorithm to control the overall simulation. The timestep was equal to 10% of the shedding period (f = 400 Hz, Ts = 0.25 ms) and the second-order implicit scheme was used for temporal discretization. The default coefficients and relaxation factors were kept. The shedding cycle fully developed over the first 0.1 s and the simulations were continued for another 0.1 s, which was sufficient for multiple fully developed vortices to shed and interact with the grid. The fluid was modeled as constant-density standard air (T = 20 °C, P = 101.3 kPa). Compressibility effects were neglected because the Mach number was far below 0.3. The inlet was modeled as a velocity inlet and the outlet as a pressure outlet. The inlet velocity was fixed to 10 m/s (Re_{BB} = 3200, Re_{Pipe} = 32,000). The walls (wall, bluff body, and grids) were modeled as a

no-slip boundary condition. The 2-layer all-Y+ method was used for all the wall treatments, with a minimum distance of 0.001 mm [14].

Force sensors were added to the bluff body and the grids to monitor the lift and drag acting on them. In addition, surface-averaging planes and grids of points, located on the virtual planes (Figure 1: P_{M1}, P_{M2}, P_{M3}, and XY cross plane), monitored the total pressure, TKE, velocity, and vorticity. The surface-averaging planes recorded the mean intensity, standard deviation, and uniformity.

2.4. Mesh Design

The mesh, shown in Figure 2, was generated using a polyhedral mesher with three optimization cycles. The global cell size is 5% of tunnel diameter (D) and the core region of interest is refined to $0.02D$ (1.0 mm). The refinement zone starts $4d$ (20.0 mm) upstream of the bluff body and extends to P_{M2}. It spans the entire width of the cylinder and $\pm 2d$ radially ($\pm$10.0 mm). The surface size of the bluff body is $0.05d$ (0.1 mm), with a max cell size of $0.1d$ (0.5 mm) in its wake, defined by a tapered region spanning the width of the cylinder and extending up to the grids. The surface size of the wires is 0.065 mm (ensuring at least 8 points on the circular perimeter of the smallest grid), with a max cell size of $0.1d$ (0.5 mm) in the wake, defined by a tapered region spanning the width of the cylinder and extending up to P_{M2}. The wall mesh merges with the global mesh over six prism layers at a growth rate of 1.3. The Y+ for the bluff body and grids is less than 0.5, and the Y+ for the pipe is less than 1.5 in the region of interest.

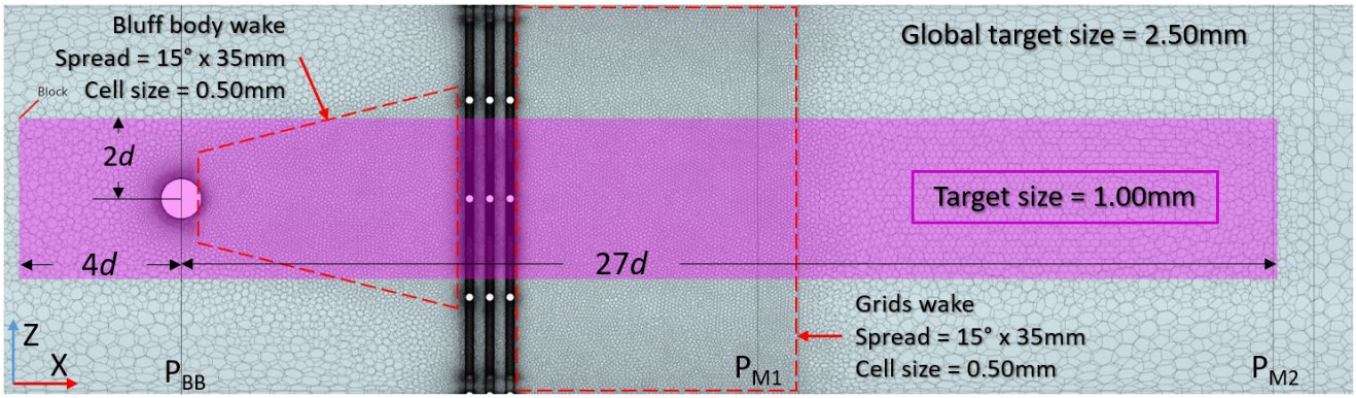

Figure 2. Mesh and refinement zones.

The mesh parameters were selected following a convergence study presented in Appendix A.

2.5. Design of Experiment

The design of experiment (DoE) was planned to understand how the grid wire diameter (d_w), the grid porosity (φ), and the inter-grid spacing (ε) influence vortex breakdown. Porosity describes the void ratio of a structure. When looking at grid from the front, the porosity is given by $\frac{a \cdot b}{A \cdot B}$, where $a \cdot b$ is the open area and $A \cdot B$ is the total cell area. Figure 3 presents the grid variables. The grids used in this study have a square opening; hence, $A = B$. Note that $A = a + d_w$.

Three different wire sizes (0.25, 0.50, and 1.00 mm) and three nominal porosities (55, 70, and 85%) were tested. In addition to single-grid configurations, stacks composed of three grids were considered with an inter-grid spacing (ε) equal to 0.5×, 1.0×, and 1.5× the bluff body diameter (2.5, 5.0, and 7.5 mm).

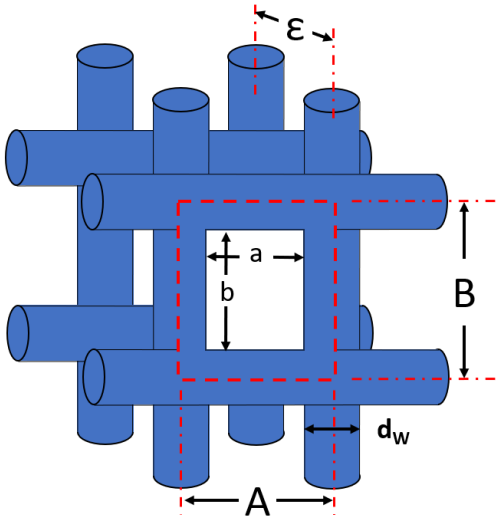

Figure 3. Grid parameters.

The lower limit for the wire diameter (d_w) was 0.25 mm because results from previous authors [3] showed that a finer grid would likely be ineffective. The upper limit for the d_w was 1.00 mm, as it needed to be relatively small compared to the vortex-seeding bluff body diameter, so as to not generate its own large vortices downstream. Since the overarching goal is to develop a solution causing a lower pressure loss than metallic foam, the low end of the porosity range was set to φ = 55%. The upper end of the porosity range was set to φ = 85% to ensure that the grid opening (dimensions a and b in Figure 3) remains below 2.5d. The lower bound of the inter-grid spacing (ε) needs to be sufficiently large to avoid creating channels between the grids. The upper bound of the inter-grid spacing ensures that the thickness of a stack of 5 × 1.00 mm grids will not exceed 25 mm (design-bound).

The nomenclature adopted for the individual setups describes the nominal wire diameter and the nominal grid porosity; e.g., D025P55 identifies a single grid with a wire diameter of 0.25 mm and a porosity of 55%. For configurations with multiple grids, a suffix describes the number of grids and the inter-grid spacing (ε); hence, D100P85−3x2.5 corresponds to a stack of three grids with a wire diameter of 1.00 mm, a porosity of 85%, and an inter-grid spacing of 2.5 mm. Table 2 presents the grids tested, where a is the width of a grid opening. Note that the baseline configuration refers to the case without any grids, i.e., only the tunnel and the bluff body.

Table 2. List of individual grids used in this study.

Grid	d_w [mm]	a [mm]	φ [%]
D025P55	0.25	0.71	54
D025P70		1.30	70
D025P85		3.30	86
D050P55	0.50	1.40	53
D050P70		2.59	69
D050P85		5.69	83
D100P55	1.00	3.08	55
D100P70		7.17	74
D100P85		11.25	81

The effect of the grid alignment was also investigated, as shown in Figure 4. The intent behind the misaligned arrangements was to increase the blockage area in a similar manner as would a lattice structure. For the offset grid configurations, the second grid is rotated 45° and the third grid is shifted up and right by $a/4$.

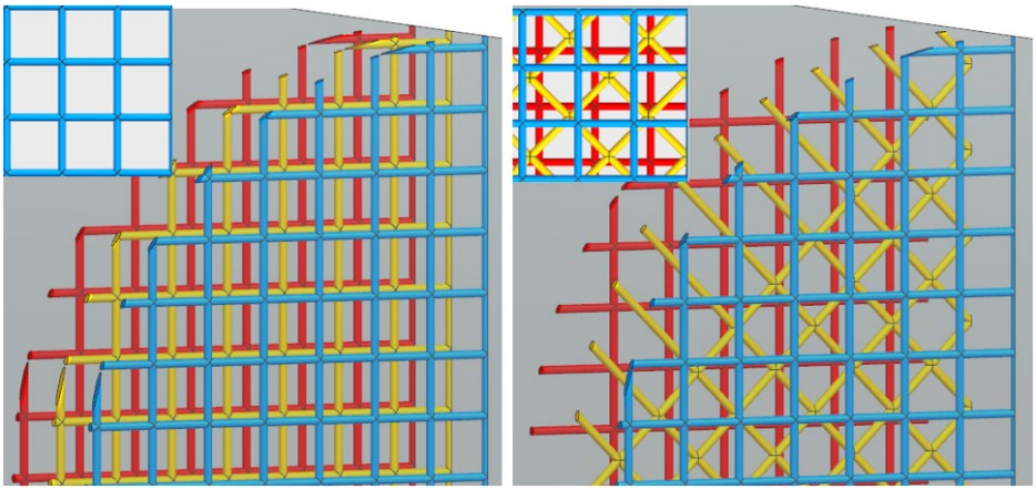

Figure 4. Grid alignment. (**Left**) Inline grids, (**right**) offset grids. The inset in the top-left corner shows the apparent porosity.

2.6. Key Performance Indicators

2.6.1. Pressure Drop

The pressure drop (ΔP) is an important metric to evaluate the efficiency of the different structures. It corresponds to the difference in pressure between a reference point and a second one located downstream. In an ideal system, the pressure at the inlet and the outlet would be the same. However, the grids create a restriction to the passage of the fluid, which results in a pressure loss. In order to maximize the overall efficiency of the engines, it is desirable to minimize the pressure drop. In this case, the pressure drop is measured between the inlet and outlet of the CFD domain (Figure 1) using surface-averaging planes. To isolate the effect of the grids, the baseline ΔP (caused by the tunnel and the bluff body, Equation (1)) is subtracted from the total ΔP measured (Equation (2)). The results for the pressure drop are averaged over 40 shedding cycles, from t = 0.1 s (when the shedding is fully developed) to t = 0.2 s (when the simulation stops).

$$\Delta P_{baseline} = \Delta P_{outlet} - \Delta P_{inlet} \text{ (without any grids)} \quad (1)$$

$$\Delta P_{grid} = (\Delta P_{outlet} - \Delta P_{inlet}) - \Delta P_{baseline} \quad (2)$$

2.6.2. Turbulent Kinetic Energy

In combustion systems, turbulence is generally a good thing because it increases the mixing rate of the fuel with the air, which results in a faster flame speed and more power [1]. A common metric to assess the turbulence level of a flow is the turbulent kinetic energy (TKE), which represents the kinetic energy per unit of mass carried by the fluctuations. The instantaneous TKE from the turbulence model was spatially averaged using a surface-averaging monitor located on the plane P_{M2}. The results were then time-averaged over 40 shedding cycles, from t = 0.1 s to t = 0.2 s. For clarity, the results are presented as a reduction in TKE relative to the baseline (configuration without the grids), and are calculated by Equation (3).

$$Relative\ TKE\ Reduction = \frac{TKE_{Grid} - TKE_{Baseline}}{TKE_{Baseline}} \quad (3)$$

2.6.3. Flow Velocity Uniformity

In the scope of delivering air to the combustor, it is highly desirable for the velocity to be as homogenous as possible to ensure the air/fuel ratio is uniform within the flow. The presence of high/low velocity streaks can result in rich or lean pockets, which opens the door to a plethora of combustion issues such as auto-ignition, noise, and high NOx

emissions [1]. This homogeneity can be quantified by calculating the flow uniformity (θ), which is a ratio of the sum of local velocity deviations relative to the mean velocity. It is calculated by Equation (4), where U_i is the instantaneous local velocity at a given point, $\overline{U}$ is the surface-averaged velocity, and n is the number of points sampled [15]. For an ideal flow without any deviation, $\theta = 1$.

$$\theta = 1 - \frac{\sum|U_i - \overline{U}|}{n|\overline{U}|} \tag{4}$$

The local velocities are sampled on an array of points located on plane P_{M1} with a resolution of 50 × 10 pts. An exclusion filter is applied to remove the points which lie within 2 mm of the tunnel wall to avoid boundary-layer effects. The results for the flow velocity uniformity are averaged over 40 shedding cycles, from t = 0.1 s (when the shedding is fully developed) to t = 0.2 s (when the simulation stops).

Note that the flow upstream of the grids follows an M-shaped profile due to the blockage created by the bluff body. Since the fluid is incompressible, the fluid must accelerate around the bluff body, resulting in a maximum velocity higher than the nominal speed. This profile is consistent with the results from Ong and Wallace [16]. As a result, the flow field uniformity upstream of the grids is around 90%.

2.6.4. Transmitted Vortex Size

The last KPI is the transmitted vortex size (TVS), which is estimated by visualizing the eddies with an isosurface of the Q-criterion (Q = 5000 s^{-2}). The vorticity for i (around the x-axis) is overlayed on the isosurface. For clarity, the visible region is bound between 20 s^{-1} and 300 s^{-1}.

The Q-criterion is commonly used to identify and visualize vortical structures in CFD. By defining an isosurface as a function of the Q-criterion, one can quickly "adjust" the detection threshold of the vortices. Selecting the correct Q-criterion value comes down to which structure is of interest. In this case, Q = 5000 s^{-2} is adequate because it is sufficiently sensitive to identify the TVS up to the second plane of measurement (PM2 in Figure 2) without capturing the smaller, secondary vortices. The main caveat of this method is that it does not capture the energy of the vortex. However, the authors believe that using the Q-criterion is a valid method for a comparative study like this one, since the isosurface is defined with the same threshold, and the mesh cell sizes are the same for all simulations.

The estimation of the size of the vortical structures was simplified by measuring their cross-section at the symmetry plane. By the time the transmitted vortices reach P_{M2}, they are strongly coherent structures and perpendicular to the flow direction, as evidenced in the next figure. Their cross-section is therefore a meaningful characteristic dimension. The size of the vortices is manually measured using an image processing software. The pixel/mm ratio is calculated by measuring the diameter of the tube, which is a known dimension. Because the vortices are more ellipsoid than circular, the length of the minor and major axis are measured, and the area is calculated. The diameter of the vortex is then calculated from the ellipse area. This is a simplification to facilitate the comparison between the cases. The vortices are measured at a distance of 2.25D (115 mm) downstream of the last grid, under the same meshing conditions, to keep the diffusion length similar between the cases. Figure 5 shows the transmitted vortices for the baseline (top) and D100P55−3x5.0 (bottom) configurations. The results are measured for a single timestamp between T = 0.19 and 0.20 s, when the trailing edge of the vortex lines up with $P_{M2'}$.

The shedding is periodic, and the breakdown and reformation patterns of the vortices are very similar over time. The vortex size was initially measured systematically for every timestep where the vortex intersected PM2 between t = 0.175 s and t = 0.200 s, for a total of 11 points per series. It was quickly determined that the variation in the vortex size was negligible (±3%). The authors therefore concluded that it is acceptable to measure the vortex size for a single instance.

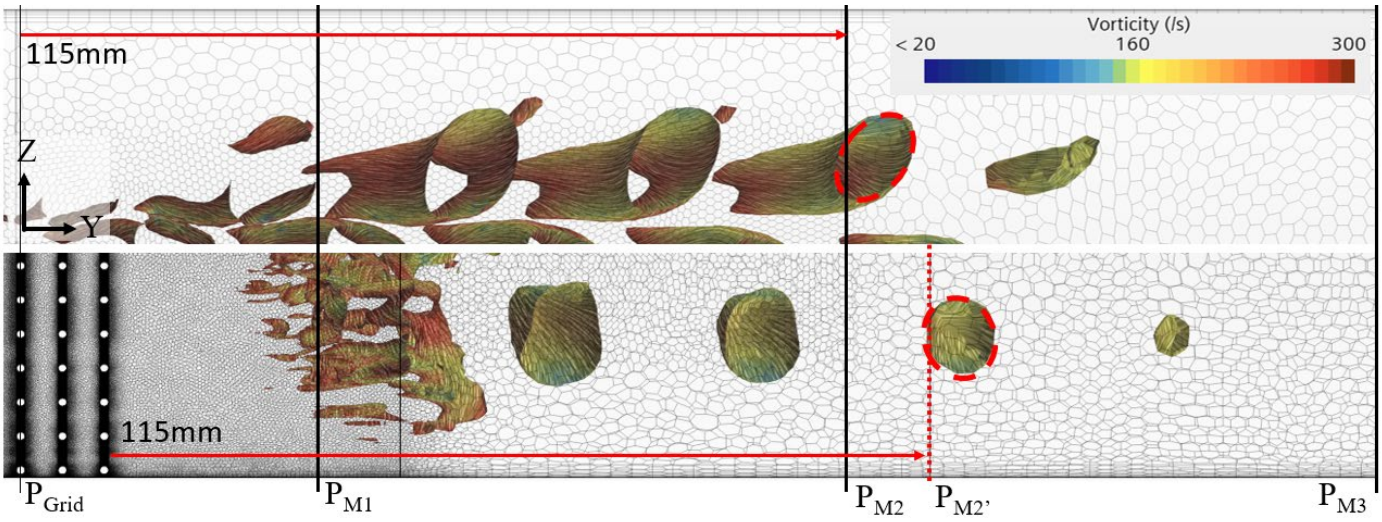

Figure 5. Isosurface of the Q-Criterion showing the vorticity. Top: baseline; bottom: D100P55−3x5.0.

3. Results

The simulations described in Table 1 were performed and analyzed systematically using the four KPIs described in Section 2.6. The results are presented and interpreted in the flowing section.

3.1. Pressure Drop

The variation in the pressure drop, computed with Equation (2), as a function of the inter-grid spacing is presented in Figure 6 for two porosities (a = 55% and b = 85%). The solid lines correspond to the cases where the grids are inline; the dashed lines correspond to cases where the grids are misaligned (offset). In addition to the three spacings tested (ε = 2.5, 5.0, and 7.5 mm), a fourth column (INF) is added, which extrapolates the results if the three grids are infinitely separated by multiplying the pressure drop from the individual grid cases by three.

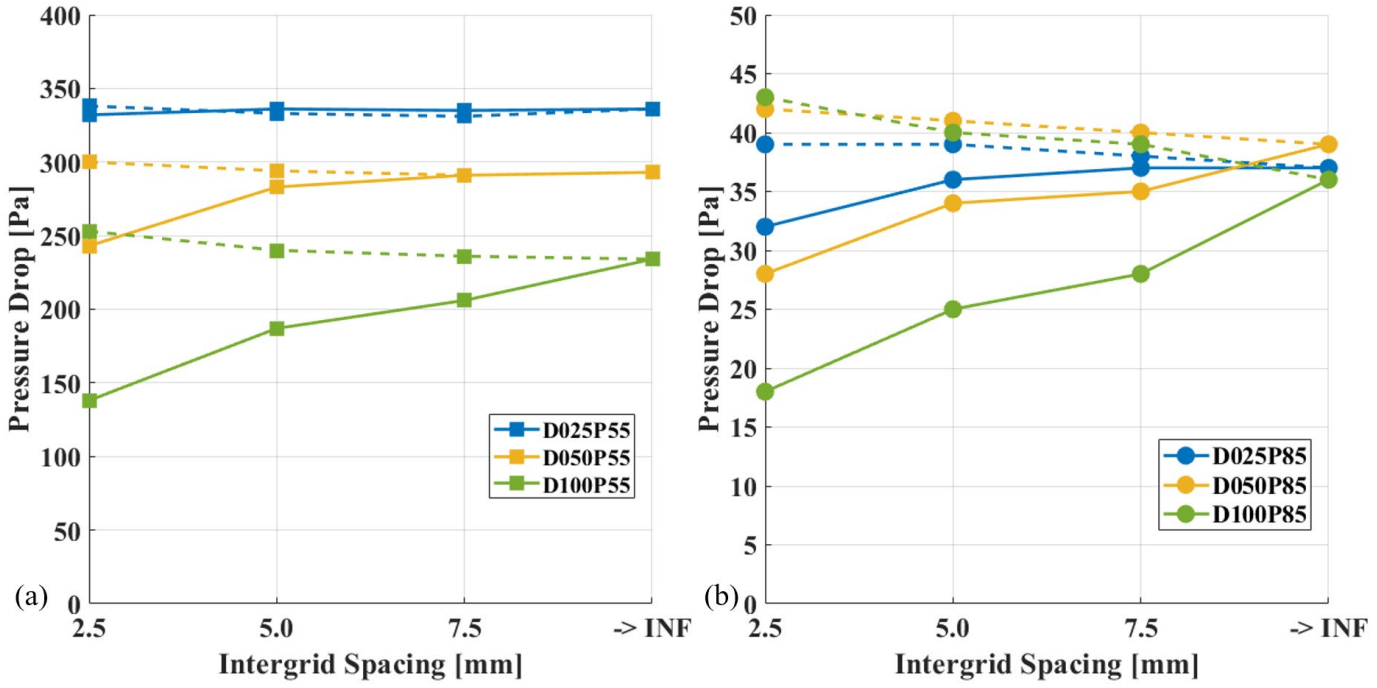

Figure 6. ΔP evolution vs. inter-grid spacing. (**a**) φ = 55%; (**b**) φ = 85%. Solid lines = inline; dashed lines = offset configurations.

Looking at Figure 6, three things stand out. First, porosity has a massive effect on the pressure drop. For a given wire size, increasing the porosity from 55% to 85% leads to a 7–10× reduction in the pressure drop. The effect of the porosity is straightforward; a more porous structure creates less blockage, which results in lower losses. Second, for a given porosity, increasing the wire diameter seems to help minimize the pressure losses, and this trend is amplified when the inter-grid spacing is narrow. When ε = 2.5 mm, the pressure drop for the largest grids (D100, green) is about half that of the smallest grids (D025, blue). This is likely because the smaller grids have more wires in the flow, which increases the amount of interaction with the flow. For reference, D025P55 contains 54 struts vs. 16 struts for D100P55. Third, as the space between the grids increases, the interaction between them diminishes until it becomes negligeable, eventually acting as independent grids. At this point, the blockage experienced by the air is solely a function of the blockage area of the individual screens. Notice that when the grids are aligned (solid lines), a lower ΔP is achieved by decreasing ε, but the effect of the inter-grid spacing reverses with the offset grid alignment, such that, when the grids are offset (dashed lines), a lower ΔP is achieved by increasing ε.

Figures 7–9 show the instantaneous total pressure at the symmetry plane for different grid configurations, exposing the effect of the grid wire diameter and inter-grid spacing on the wake generated, which helps to explain the results.

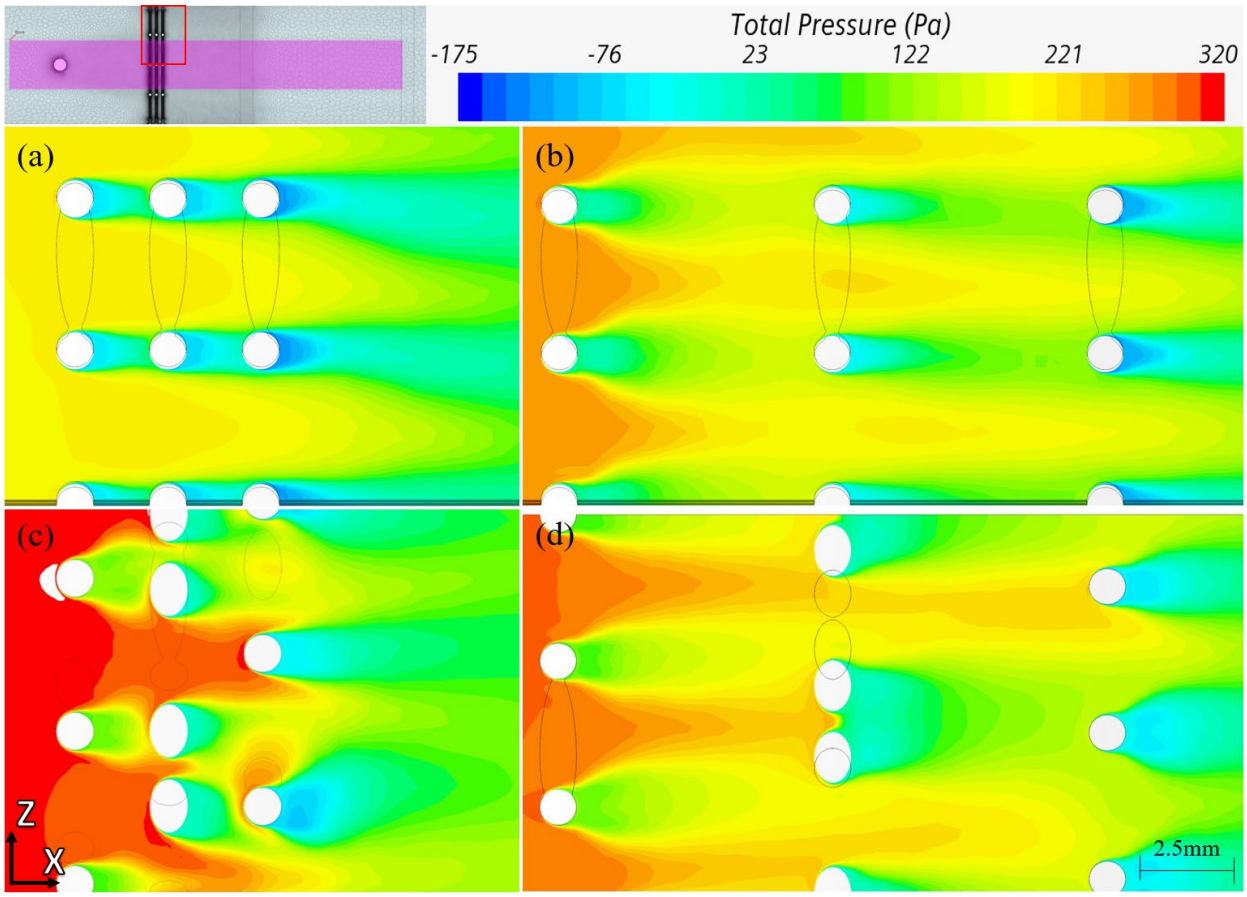

Figure 7. Instantaneous total pressure field at the symmetry plane for (**a**) D100P55−3x2.5 inline, (**b**) D100P55−3x7.5 inline, (**c**) D100P55−3x2.5 offset, and (**d**) D100P55−3x7.5 offset.

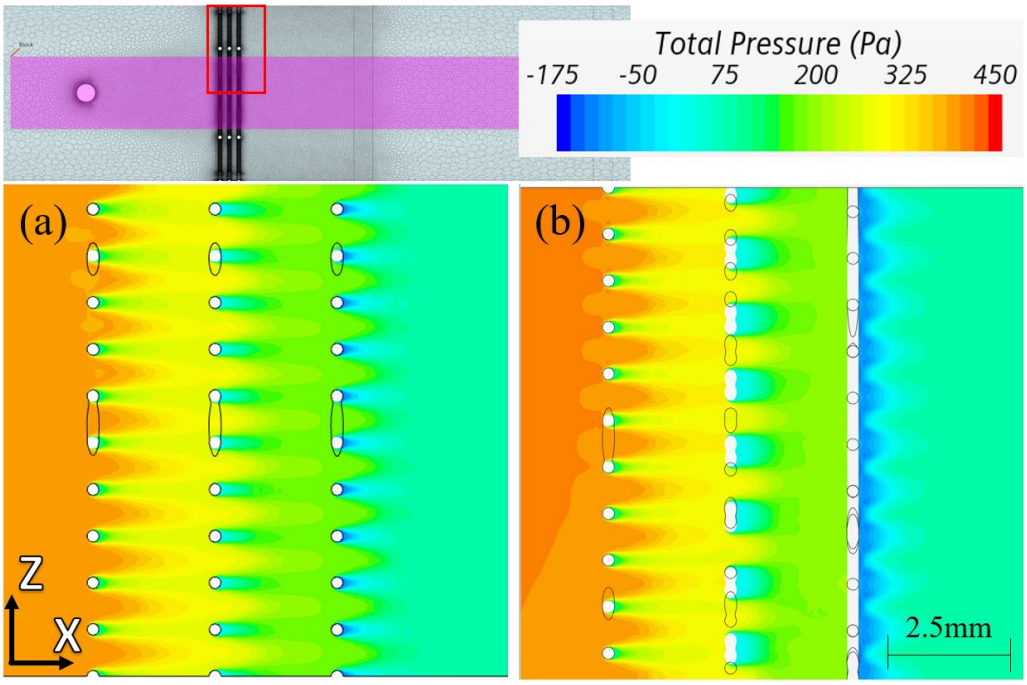

Figure 8. Instantaneous total pressure field at the symmetry plane for D025P55−3x2.5: (**a**) aligned grids, (**b**) offset grids.

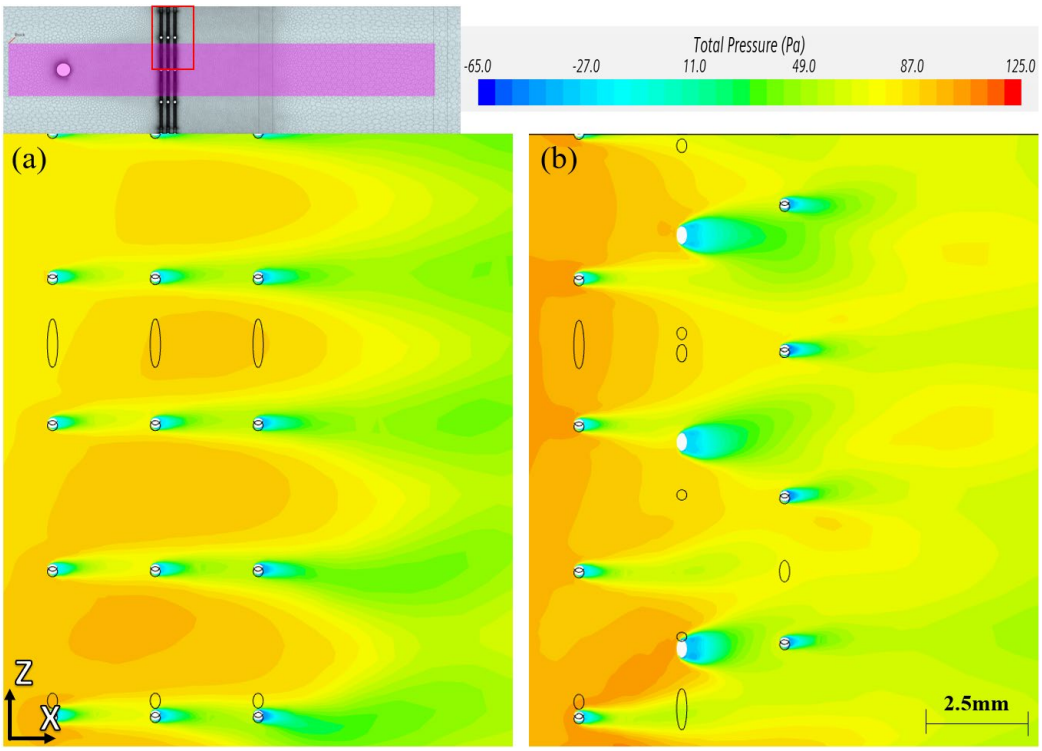

Figure 9. Instantaneous total pressure field at the symmetry plane for D025P85−3x2.5: (**a**) aligned grids, (**b**) offset grids.

The wake, which causes a decrease in the total pressure, is clearly visible behind each wire and is responsible for the pressure loss. When the screens are aligned, reducing ε allows the wake of the first grid to extend to the next one (Figure 7a), maximizing the drafting effect, which leads to a lower pressure drop. The same principle is often observed in sports such as cycling, where athletes follow each other very closely to benefit from the

slipstream. As the gap increases, the strength of the wake diminishes (Figure 7b) and the pressure field downstream becomes more uniform. When ε is large, the interaction between the grids is negligible and the effect of each grid is independent from those upstream.

When the grids are misaligned, this slipstream effect does not come into action because the grids downstream do not nest in the wake formed by the ones upstream, no matter how close they are. In addition, randomly arranging the grids increases the visible blockage area as the screens downstream come into view, which effectively reduces the apparent porosity of the stacks. With the offset configuration, reducing ε causes the ΔP to increase because the flow must not only bypass the grids, but is also forced to interact with the wake created by those upstream (Figure 7c). On the other hand, increasing ε diminishes the interaction between the grids until they become independent, at which point the grid arrangement becomes irrelevant (Figure 7d).

Because the size of the wake varies with the wire diameter, the effect of the spacing is intimately related to the screen size. The porosity also has an effect on the wake. Looking at Figure 8, the wires are so close to one another that the low-pressure regions they create all coalesce together before reaching the next grid, even in the most compact configuration. This explains why neither the grid alignment nor the inter-grid spacing had a meaningful impact on the pressure loss for the D025P55 cases in Figure 6a.

Increasing the porosity creates larger gaps between the wires, which allow the wakes to form independently. The pressure distribution between Figures 8 and 9 is noticeably different, especially when the grids are misaligned, which explains the results for the D025P85 cases in Figure 6b.

It is worth noting that the offset grid configurations yield a more uniform total pressure field downstream due to the interactions phasing out. This is particularly visible in Figure 9, where the regular grid placement (left) causes the wakes to deepen rather than to diffuse. The same observations can be made for the compact configurations in Figure 7a,c. However, increasing ε dampens this homogenizing effect since it reduces the interaction level between the grids (Figure 7b,d).

3.2. Turbulent Kinetic Energy

Figure 10 presents the reduction in TKE relative to the baseline (configuration without the grids), calculated by Equation (3), as a function of the inter-grid spacing. Note that the first column presents the results for the individual grid configurations. Again, the results are presented for two porosities (a = 55%, b = 85%), and the solid lines correspond to the inline configurations and the dashed lines correspond to the offset configurations.

Looking at Figure 10, the first thing that stands out is that the coarser grid configurations (D100—green) have systematically higher TKE levels than their finer alternatives (D025—blue and D050—yellow). Overall, the configurations with a single grid are remarkably effective at damping the turbulences.

When the porosity is low (Figure 10a), the introduction of additional grids initially leads to a dip in the TKE reduction, but the smaller grids eventually recover as ε increases. When the porosity is large (Figure 10b), the introduction of the additional grids has a negligible effect at first for the finer grids, but eventually leads to a slight improvement as ε increases. On the other hand, increasing ε for the coarser grids always results in a higher TKE level, regardless of the porosity. Another key trend is that the offset grid configurations systematically improve the TKE reduction over the aligned configurations. When the porosity is high, the additional grids significantly improve the TKE reduction if they are in the offset configuration, but have a negligible effect if they are inline. Looking at Figure 10, the gap between the aligned and offset configurations (solid vs. dashed lines) is significantly larger on the right graph (φ = 85%) compared to the left graph (φ = 55%), and this effect is amplified by increasing the wire diameter (D025—blue vs. D100—green).

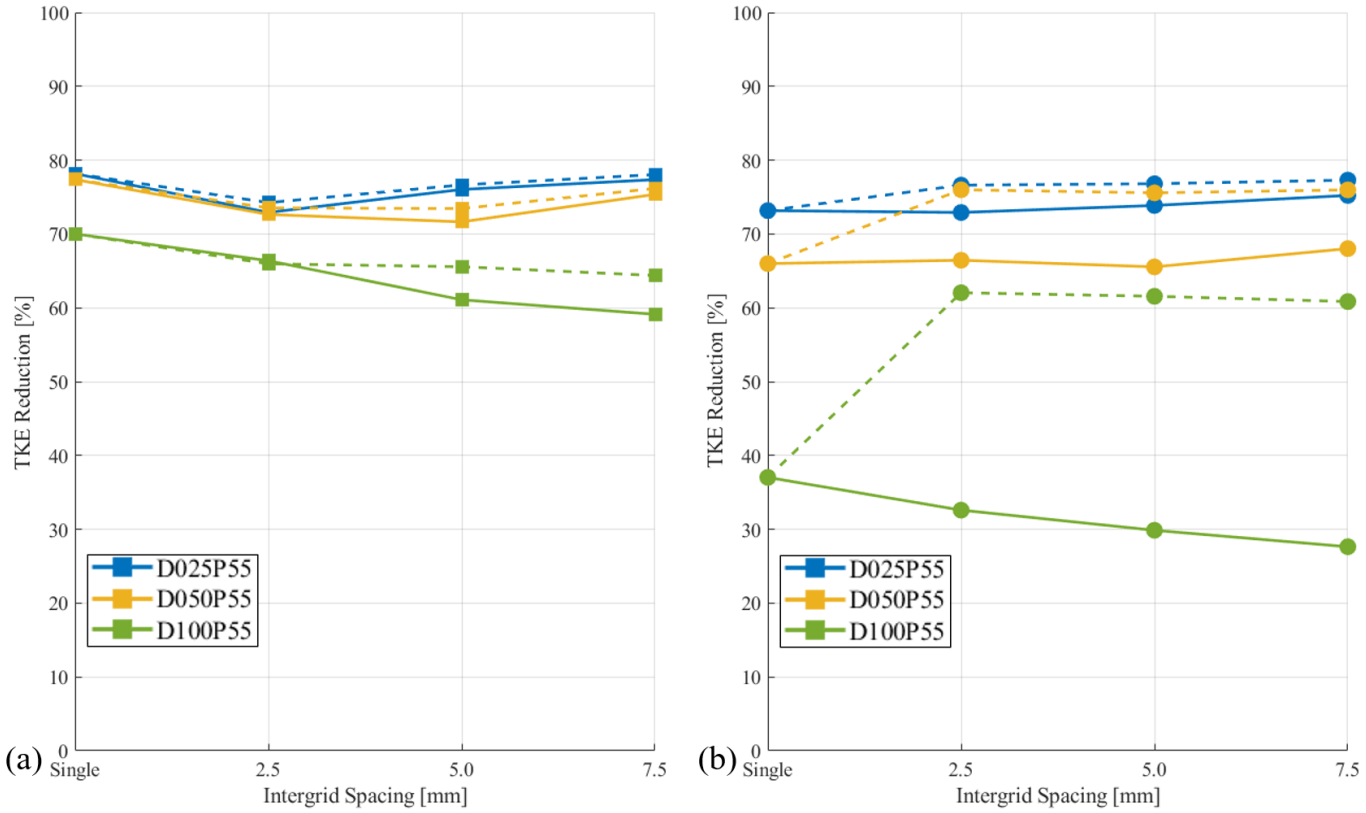

Figure 10. TKE reduction vs. inter-grid spacing. (**a**) φ = 55%; (**b**) φ = 85%. Solid lines = inline; dashed lines = offset configurations.

The effect of the grids on the TKE is perhaps not as straightforward as it was for the pressure drop because two competing mechanisms are at play. The first one is the disruption of the incident vortex by the grids, which reduces the transmitted TKE. This is mostly a function of the grid porosity, because the more porous a grid is, the less interaction it has with the vortex, allowing more energy to pass through. This explains why the TKE reduction levels in Figure 10a (φ = 55%) are noticeably higher than in Figure 10b (φ = 85%). The second mechanism responsible for the residual TKE is that the grids themselves create turbulence as the fluid flows around the wires, generating secondary Von Karman vortex alleys which contribute to the residual TKE levels measured. This effect is sensitive to the wire diameter, since larger wires create larger eddies, and is particularly visible in Figure 10b, where the three different wire sizes are clearly separated, especially when the grids are aligned.

Figure 11 presents the evolution of the spatially averaged TKE across the duct section (the symmetry plane) as a function of the axial distance from the inlet for the D025−3x7.5 configurations for two porosities (φ = 55%, purple; 85%, orange). The dashed lines correspond to the offset configurations. The grids introduce a lot of turbulence, especially when the grids are very restrictive, but it quickly decays.

Figure 11 highlights three key aspects of the TKE evolution over the axial distance. First, the TKE increases around the 200 mm mark as the air flows around the bluff body, creating the Von Karman street effect. The TKE intensity then plateaus for all the conditions until they reach the grids. Second, as the fluid progresses further downstream, it interacts with the grids. This gives rise to a second increase in turbulent kinetic energy due to the formation of secondary vortices caused by flow around the grids. Because the grids in Figure 11 are quite small, the secondary vortices they create are also small and therefore dissipate quickly, which explains the abrupt variations in TKE levels. The more restrictive the grid is, the steeper this effect will be, since a less porous grid will have more wires in the flow, which obviously creates more secondary vortices. Since the flow is incompressible, it

must accelerate as it passes through the screen openings, which further contributes to the intensity of the secondary vortices. Finally, the incident vortex is distorted as it interacts with the grids. This leads to a dissipation of some of the turbulent energy retained by the transmitted vortex, as evidenced by the progressively lower minima of the TKE past each grid. In contrast, the baseline configuration (without the grids) experiences a slow and steady decay of the TKE.

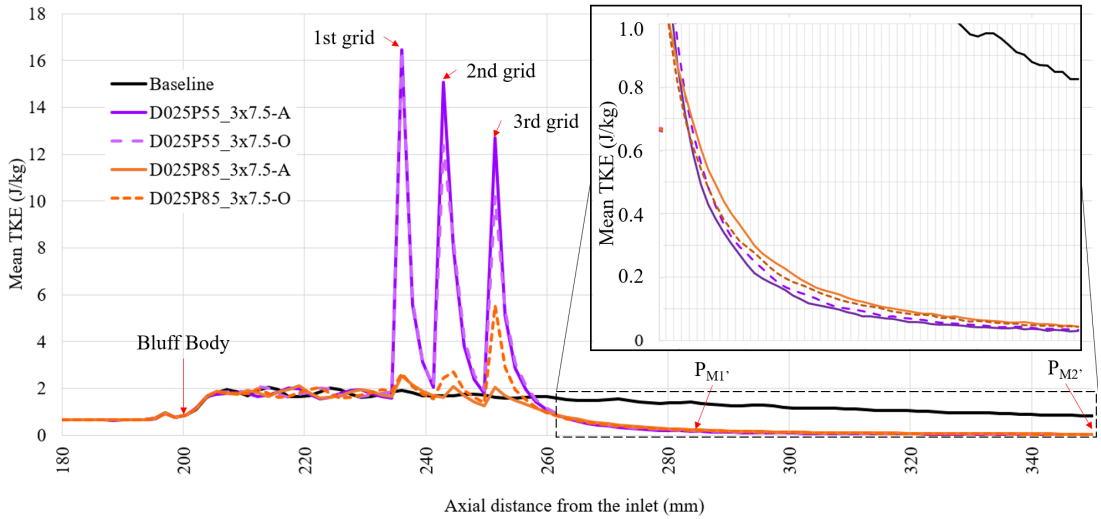

Figure 11. Evolution of the average TKE at the symmetry plane as a function of the axial distance for the D025 configurations.

Figures 12 and 13 show the TKE distribution along the tunnel symmetry planes for different grid configurations. On the left side, φ = 55%, and on the right side, φ = 85%. The top row shows the inline configurations, while the bottom row shows the offset configurations. The regions where the TKE exceeds 30 J/kg are clipped for clarity.

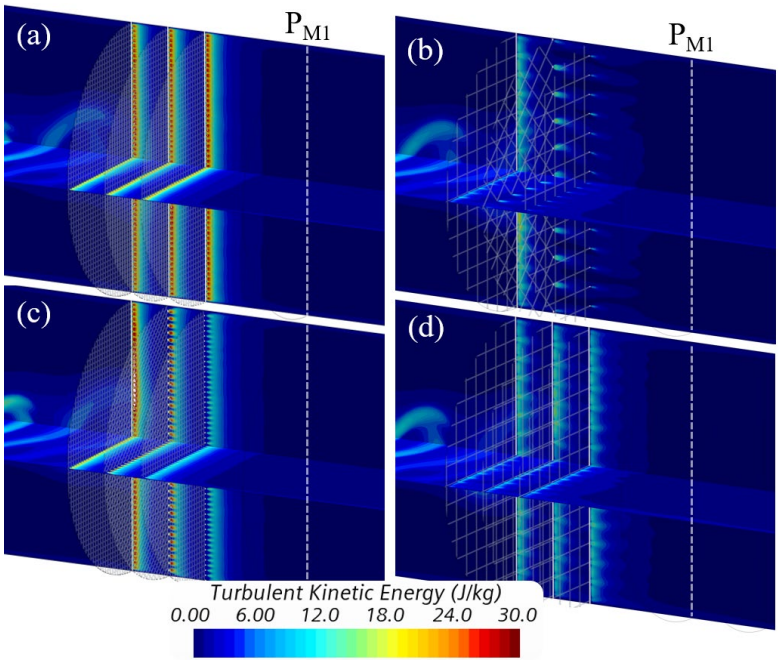

Figure 12. TKE intensity for D025−3x7.5 configurations: top row = inline; bottom row = offset; left: φ = 55%; right: φ = 85%. (**a**) D025P55−3x7.5 aligned, (**b**) D025P85−3x7.5 aligned, (**c**) D025P55−3x7.5 offset, and (**d**) D025P85−3x7.5 offset.

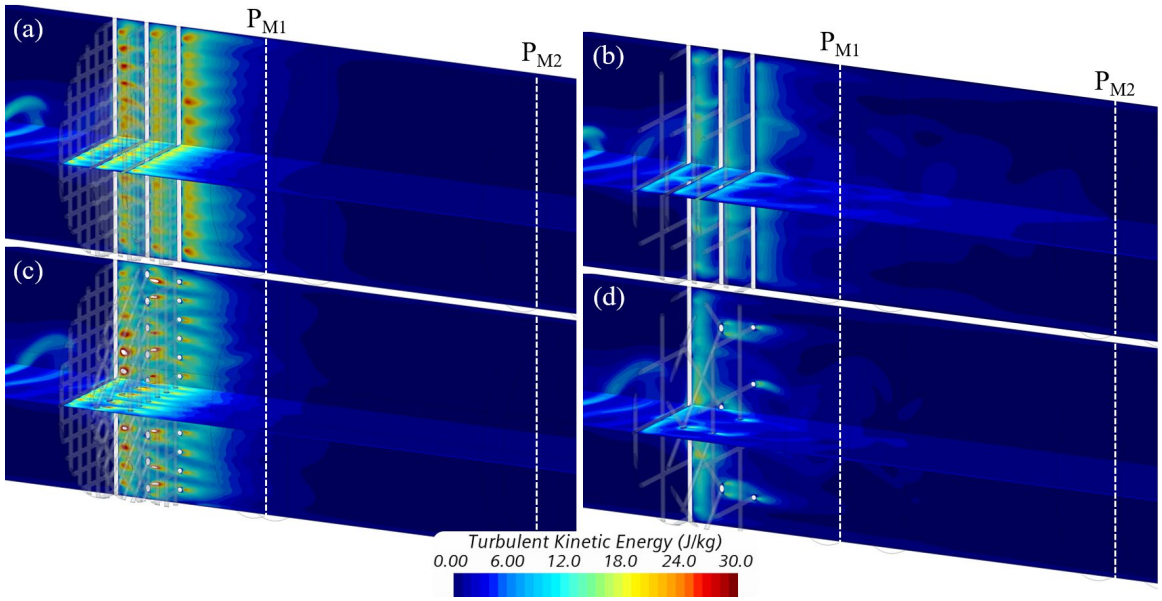

Figure 13. TKE intensity for D100−3x7.5 configurations: top row = inline; bottom row = offset; left: φ = 55%; right: φ = 85%. (**a**) D100P55−3x7.5 aligned, (**b**) D100P85−3x7.5 aligned, (**c**) D100P55−3x7.5 offset, and (**d**) D100P85−3x7.5 offset.

The results for the finest grid (D025, Figure 12) are reminiscent of Figures 8 and 9, with the wakes coalescing together for the low-porosity cases, but developing independently when the porosity is large. For the D025P55 cases, the TKE profile is uniform beyond the grids, which indicates that the turbulence caused by the incident vortex is completely dissipated and the flow is homogenous. In contrast, the D025P85 cases feature a hump in the middle region, which suggests that at least some of the turbulence from the shed vortices is transmitted through the most porous stacks. The TKE also extends further downstream.

Overall, the grid alignment appears to have a limited impact on the TKE decay. For the lowest porosity cases (D025P55, Figure 12a,c), it is impossible to tell which is inline and which is misaligned, and the difference is marginal for the most porous configurations (D025P55, Figure 12b,d). This suggests that the first grid does most of the work in terms of breaking down the vortex and dissipating its energy. This is clearly demonstrated in Figure 11.

Shifting our attention to the larger-diameter TKE maps shown in Figure 13, two things stand out. First, the TKE level for the D100P55 cases (a/c) is significantly higher near the grids than it is for its more porous counterpart (b/d). This is a consequence of the blockage created by the grids, which forces the flow to accelerate as it passes through the stacks. Second, the TKE decays much faster when the grids are misaligned, especially when the porosity is large. As explained in the last section, the wake created by the larger wires is wider and extends further downstream. When the grids are aligned, this low-pressure zone extends to the next grid, which confines the flow into channel-like structures. When the grids are misaligned, the flow becomes more chaotic and suffers from greater momentum loss, resulting in a faster TKE decay.

3.3. Flow Velocity Uniformity

The evolution of the velocity field uniformity, computed with Equation (4) on P_{M1} as a function of the inter-grid spacing, is reported in Figure 14. The graphs follow the same convention as Figure 10; i.e., Figure 10a,b present the results for φ = 55% and 85%, respectively, the solid and dashed lines correspond to the inline and offset grid arrangements, and the first column showcases the results for the individual grids.

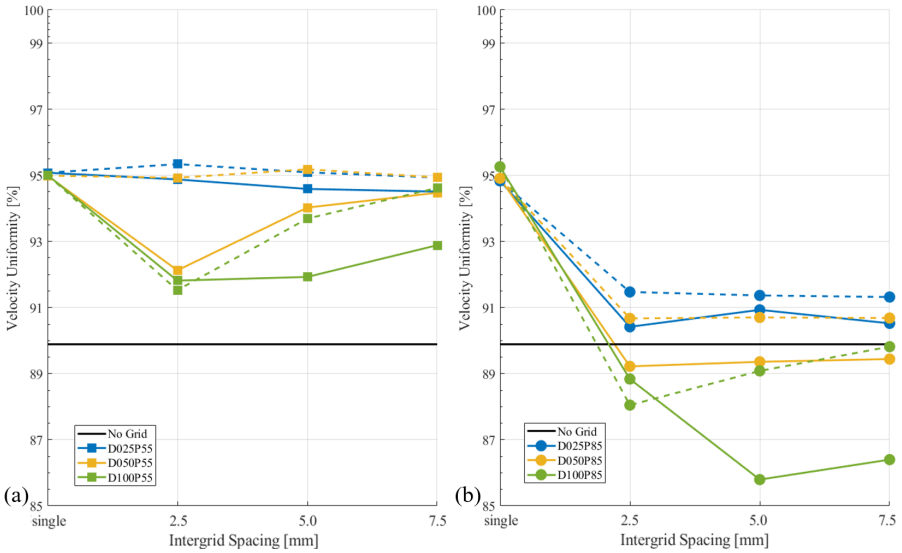

Figure 14. Velocity field uniformity vs. inter-grid spacing. (**a**) φ = 55%; (**b**) φ = 85%. Solid lines = inline; dashed lines = offset configurations. Horizontal solid line corresponds to baseline (without the grids).

Overall, the addition of the grids tends to improve the uniformity of the velocity field, but some trends still emerge. First, the velocity uniformity decreases when multiple grids are installed, compared to the single-grid configurations. Increasing the inter-grid spacing generally helps to recover some of the lost homogeneity when the porosity is low, but does little when the porosity is large, except for the coarsest grids. Next, the misaligned configurations help to homogenize the flow. Finally, increasing the wire diameter amplifies the effect of the inter-grid spacing.

The flow field is more uniform when the porosity of the grids is low and when the wire diameter is small. Increasing the wire diameter leads to stronger wakes, as seen in Section 3.1, which need a longer distance to diffuse.

Figures 15 and 16 show the velocity magnitude distribution for different grid configurations. The visible range is bounded between 0 and 23 m/s for clarity.

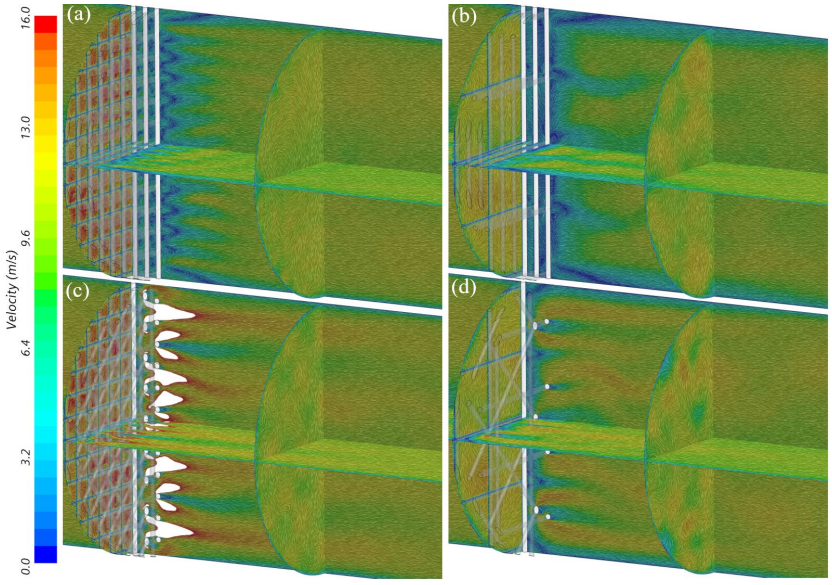

Figure 15. Flow field D100: left: φ = 55%; right: φ = 85%; top row: inline; bottom row = offset. (**a**) D100P55−3x2.5 aligned, (**b**) D100P85−3x2.5 aligned, (**c**) D100P55−3x2.5 offset, and (**d**) D100P85−3x2.5 offset.

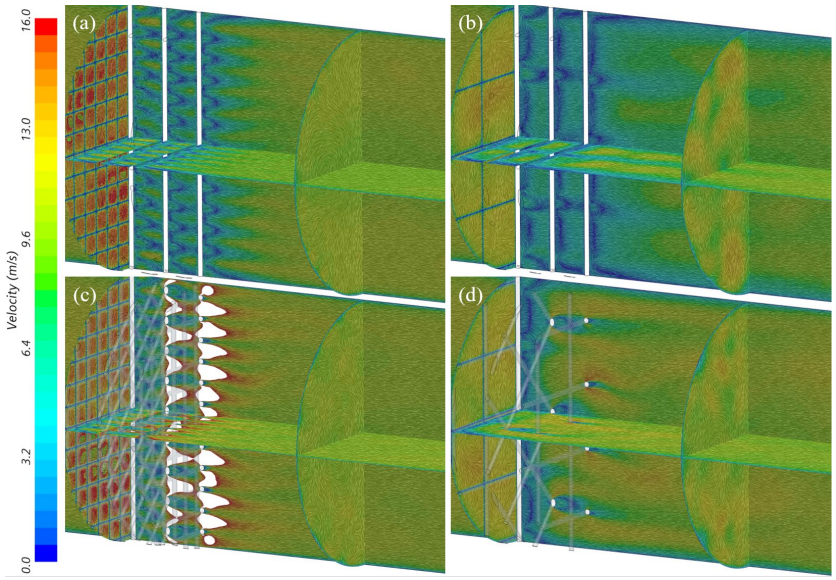

Figure 16. Flow field for D100: left: φ = 55%; right: φ = 85%; top row: inline; bottom row = offset. (**a**) D100P55−3x7.5 aligned, (**b**) D100P85−3x7.5 aligned, (**c**) D100P55−3x7.5 offset, and (**d**) D100P85−3x7.5 offset.

Looking at Figure 15 (D100, ε = 2.5 mm), the misaligned configurations seem to have a deleterious effect on the flow homogeneity, but increasing the spacing (Figure 16, ε = 7.5 mm) seems to reverse the effect of the grid alignment. When the coarser grids are aligned, they create channels which confine and accelerate the flow, and that effect is amplified by the larger inter-grid spacing. On the other hand, arranging the grids randomly increases the tortuosity, which promotes mixing. When the inter-grid spacing is small, the change in direction can be quite sharp, leading to local pockets of high-velocity intensity. Increasing the gap allows the flow to diffuse, leading to a more uniform distribution. This was also observed in Figure 9, where the offset configurations resulted in more uniform pressure fields.

3.4. Transmitted Vortex Size

The evolution of the transmitted vortex size (TVS) as a function of the inter-grid spacing is reported in Figure 17. Again, Figure 17a,b present the results for φ = 55% and 85%, respectively, the solid and dashed lines correspond to the inline and offset grid arrangements, and the first column showcases the results for the individual grids.

Placing a single grid in the flow systematically leads to a transmitted vortex larger than the baseline condition, but adding inline grids helps to reduce the TVS. This trend is amplified by increasing the inter-grid spacing. When the porosity is large, the additional grids have a minor effect on the transmitted vortex size, especially when the grids are offset. A larger reduction in the vortex size is visible when the grids are inline, and the effect is amplified by increasing the wire diameter and the inter-grid spacing. When the porosity is low, placing additional grids leads to a significant reduction in the transmitted vortex size. If the grids are inline, the size of the transmitted vortex decreases as the inter-grid spacing increases, but the effect is opposite if the grid are misaligned, with the maximum attenuation happening when the grids are at their closest.

When the incident vortex passes through a grid, it is chopped into sub-structures. In the case of a single grid, these vortical sub-structures do not experience significant distortion and can quickly reform into a coherent structure further downstream. Both Hrynuk et al. and Musta and Kruger [2–5] noted that these intermediate vortices tend to diffuse radially outward. When these sub-structures reform, the resulting vortex is larger than it was initially.

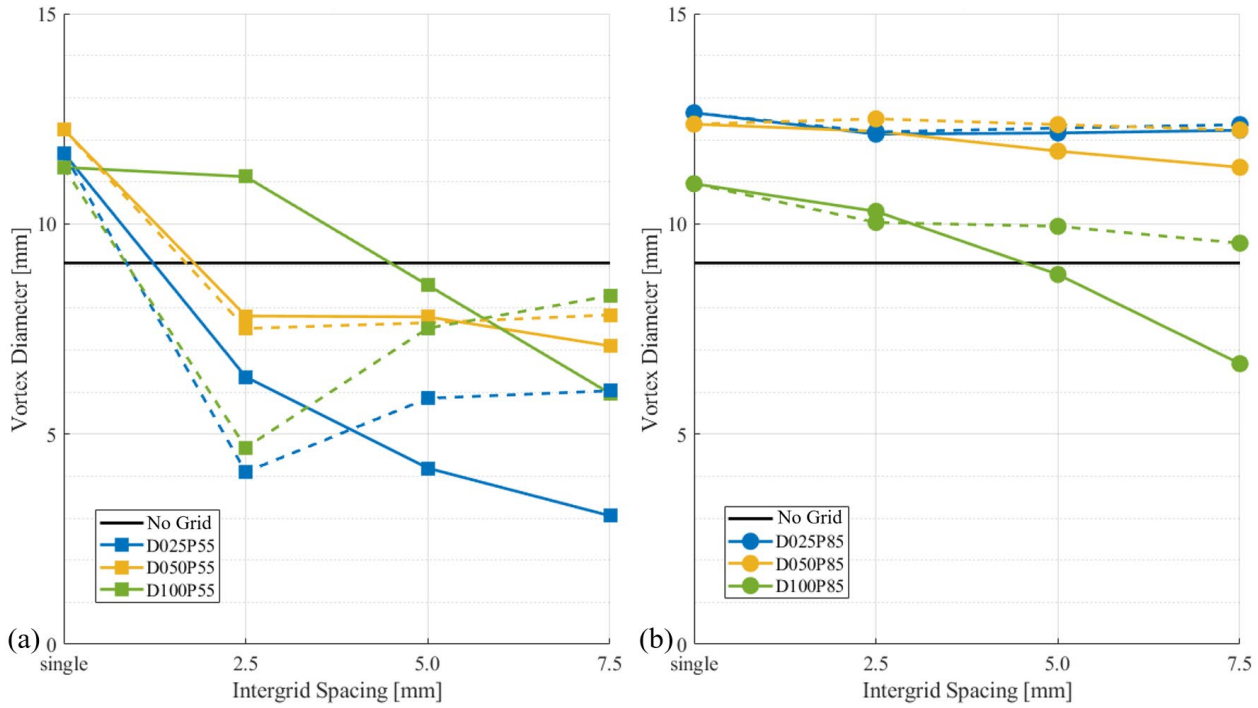

Figure 17. Transmitted vortex size vs. inter-grid spacing. (**a**) φ = 55%; (**b**) φ = 85%. Solid lines = inline; dashed lines = offset configurations. Horizontal solid line corresponds to baseline (without the grids).

When the incident vortex passes through a stack of grids, the vortical sub-structures can be exposed to a greater level of distortion, especially when the porosity is low and/or when the wire diameter is large. Partial reformation and annihilation of the transmitted vortex due to severe distortion was observed by Hrynuk et al. and Musta and Kruger [2–5].

4. Case Study

To design optimal grid stackings, a design of experiment was developed to understand how the fundamental design parameters affect the vortex-breakdown performance of a regular lattice structure. The investigation was simplified by stacking individual planar regular grids in series and varying their diameter, porosity, spacing, and alignment.

Four key performance indicators are monitored to assess the performance of the structures: the pressure drop, the residual TKE, the flow uniformity, and the transmitted vortex size. The knowledge gained through this systemic approach, presented in Section 3, will provide cues to guide the design process.

The first step is to rearrange the results in a series of influence maps where the KPIs are plotted against the wire diameter and porosity for the different grid spacing configurations. Figure 18 shows an example for the vortex size.

The next step is to define the target for each KPI. Then, the regions of interest (ROIs) are delimited for each KPI, and the resulting polygons are overlayed. The common area of the ROIs defines the confined design space. Figure 19 presents an example. The targets for the KPIs were arbitrarily defined as follows: the pressure drop shall be below 150 Pa, the residual TKE intensity shall be above 0.4 J/kg, the velocity uniformity shall be above 90%, and the transmitted vortex size shall be below 6.0 mm. The resulting design space for optimization, shown in the hatched zone in Figure 19, suggests that the porosity should be between 62 and 75%, and the wire diameter should be between 0.8 and 1.0 mm.

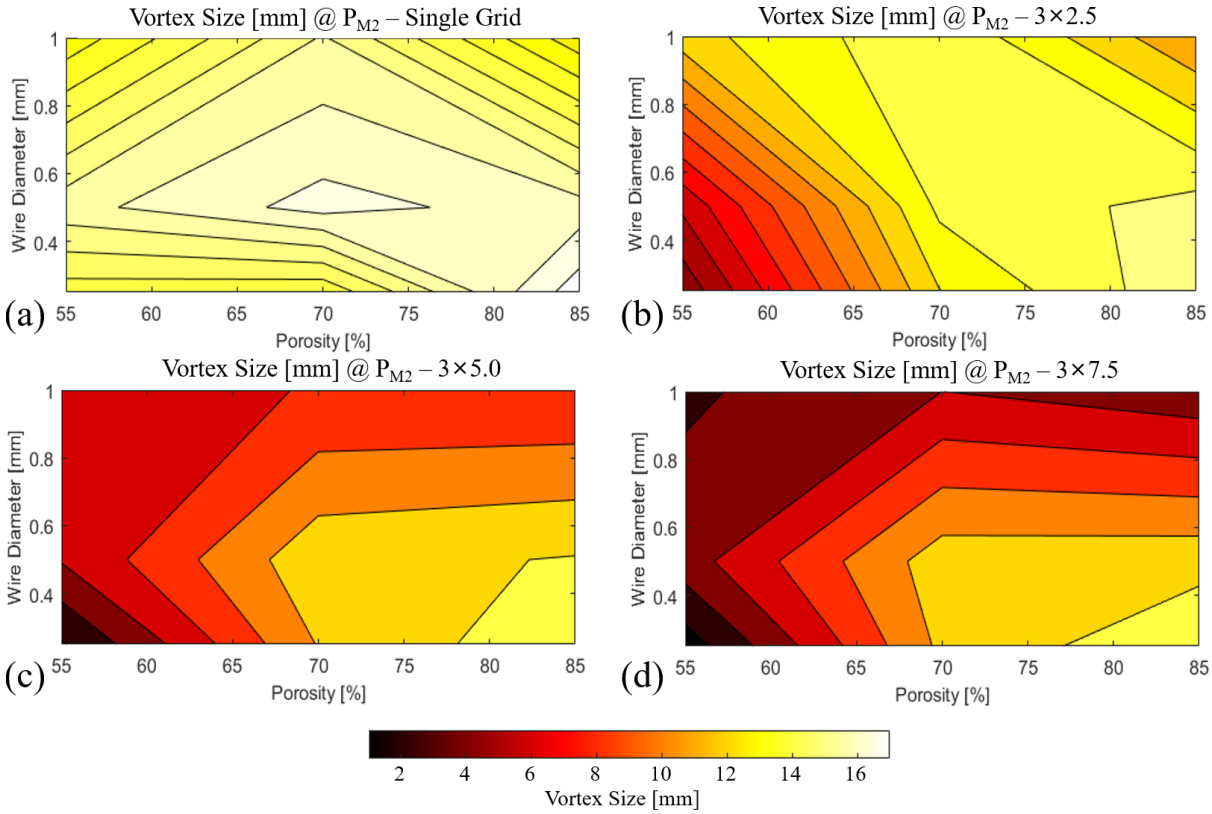

Figure 18. Influence maps of the transmitted vortex size for different grid configurations. (**a**) Single grid, (**b**) ε = 2.5 mm, (**c**) ε = 5.0 mm, and (**d**) ε = 7.5 mm.

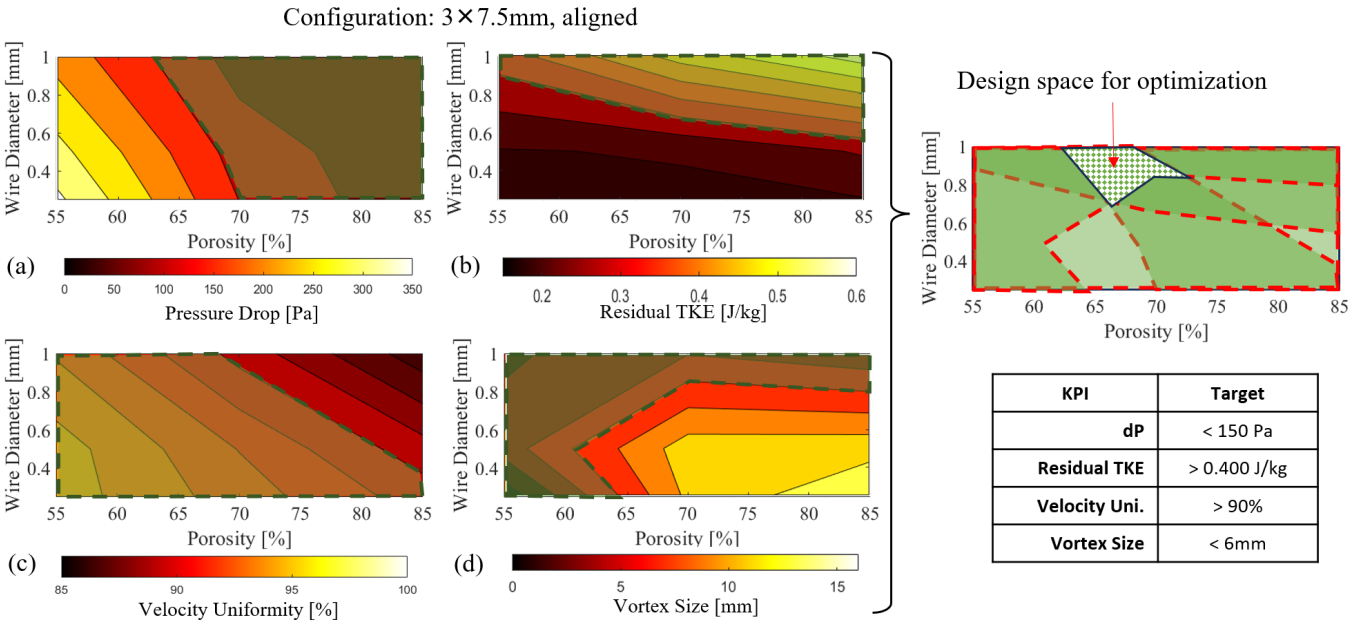

Figure 19. (**Left**): Influence maps for (**a**) pressure drop, (**b**) residual TKE, (**c**) velocity uniformity, (**d**) transmitted vortex size. (**Right**): Corresponding design space for optimization.

Balancing these requirements (trade-offs) necessitates a good understanding of the objectives of a specific application. In the use-case example presented, the main requirement is to limit the size of the transmitted vortex to 6.0 mm. Since this is a functional requirement, any solution that fails this target must be disregarded. Looking only at Figure 17, the ideal solution would be D025P55−3x7.5—inline. This option also maximizes the flow field

uniformity and the TKE reduction. However, this configuration is also the most restrictive one, causing the biggest pressure drop. The alternative would be D100P55−3x2.5—offset, which causes a much lower pressure drop, but allows a slightly larger TVS to pass through and is not as effective to homogenize the flow field or reduce the transmitted TKE.

Another limitation is that the maximum thickness of the grid stack may be restricted by the engine design. Such a constraint could limit the number of grids that can be integrated in the stack, or limit the inter-grid spacing. In this situation, the preferable solution would likely be to maximize the inter-grid spacing, even if it means sacrificing a grid, because each additional grid significantly increases the pressure drop, but does not really improve the TKE reduction or flow field uniformity. On the other hand, increasing the inter-grid spacing is shown to maximize the vortex-breakdown effect of the individual grids. Ultimately, the multi-criterion optimization process necessitates a weighted function.

5. Reformation Behavior

Understanding how the vortices reform beyond the grids can also provide some valuable insight. Three different reformation modes are identified and presented in Table 3, again using an isosurface of the Q-criterion (Q = 5000 s^{-2}) colored with the vorticity around the x-axis. To enhance the visualization of the vortex reformation, the visible range is extended between 100 s^{-1} and 2000 s^{-1} and a different color scale is used.

Table 3. Reformation behavior of the individual grids.

Grid	d_w [mm]	a [mm]	Reformation
D025P55	0.25	0.71	Instantaneous
D025P70	0.25	1.30	Instantaneous
D025P85	0.25	3.30	Jets
D050P55	0.50	1.40	Instantaneous
D050P70	0.50	2.59	Jets
D050P85	0.50	5.69	Chaotic, Delayed
D100P55	1.00	3.08	Jets
D100P70	1.00	7.17	Chaotic, Delayed
D100P85	1.00	11.25	Chaotic, Delayed

With the first mode, the incident vortex reforms instantly past the grids (Figure 20a). With the second mode, the incident vortex is divided into jet-like structures past the grids before reforming further downstream into a coherent structure (Figure 20b). With the third mode, the vortex is split into several chaotic sub-structures (Figure 20c). The high level of distortion significantly delays the reformation of the transmitted vortex.

It appears that the reformation mode depends on the size of the openings within the grids, i.e., the hydraulic diameter of the grid cell. The first mode (instant reformation) is observed when the grid opening is below 1.5 mm. The second mode (jets) is observed for an opening between 2.0 and 3.5 mm, while the third mode (chaotic and delayed) happens when the grid opening is larger than 5.0 mm. Note that the behavior is the same for the grid stacks.

The effect of the wire diameter on the vortex transmission and reformation is generally consistent with the results from previous studies [2,3,6–8], namely that the smaller grids will chop the vortex but allow it to reform instantly, while the larger grids will significantly distort the vortex, delaying and sometimes preventing its reformation. Additionally, increasing the wire diameter of the grids results in the shedding of secondary vortices.

In their past work [3], Hrynuk et al. also identified different reformation regimes. They initially suggested an "interaction" Reynolds number to explain the regimes, which was based on the wire diameter and factored in the grid porosity to correct the convection velocity. In a subsequent paper [2], they highlighted some issues with this approach and removed the porosity from the equation, suggesting the reformation regimes to solely be a function of the wire diameter and convection speed.

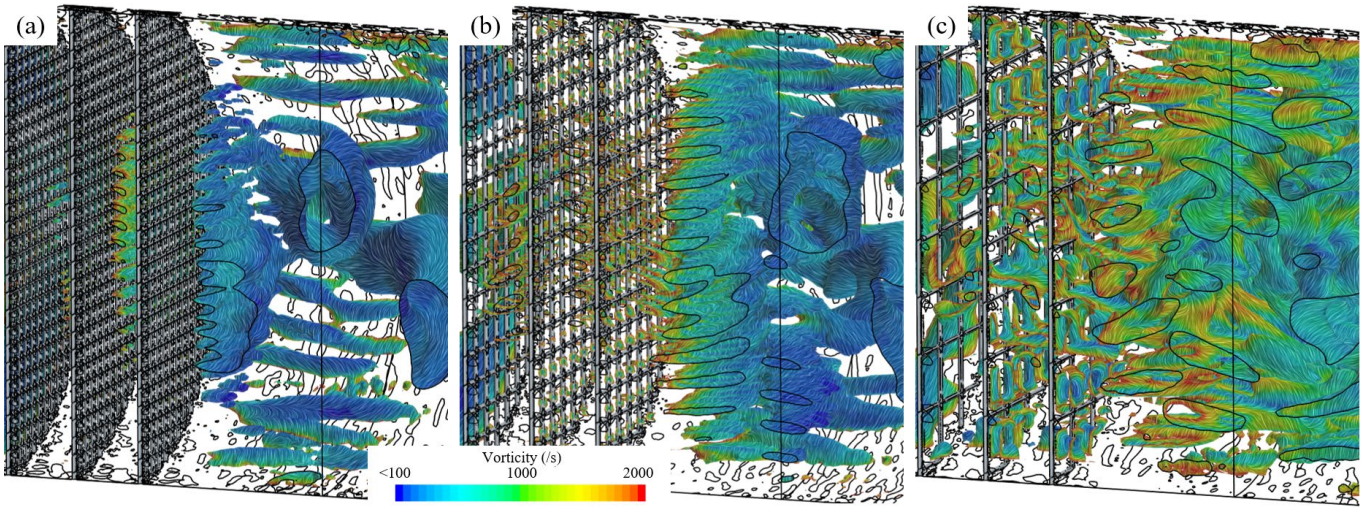

Figure 20. Reformation behavior for (**a**) D050P55−3x7.5, (**b**) D050P70−3x7.5, and (**c**) D050P85−3x7.5, using a Q-Criterion = 5000 s^{-2}.

While their model appears accurate for a pulsed vortex moving through a stationary fluid, it cannot explain the sensitivity to the grid opening clearly observed in our results. This is likely a consequence of the different approach used to generate the vortices in this experiment, which relies on a moving fluid.

6. Conclusions

This paper presents an experimental simulation protocol to systematically study the influence of four core parameters of a grid stack in the optic of developing optimized vortex-breaking porous structures, using a simple incompressible–unsteady RANS model. These parameters are the wire diameter, the porosity, the inter-grid spacing, and the grid alignment. Four metrics were identified as key performance indicators to evaluate the effectiveness and efficiency of the structures. These KPIs are the pressure drop, the residual turbulent kinetic energy, the flow field uniformity, and the size of the transmitted vortices. This investigation also proposes an approach to confine the design space in the optic of developing an optimized lattice structure.

The model relies on a Von Karman vortex street created by placing a cylindrical bluff body perpendicular to the flow inside a tunnel. Several grid stack configurations are introduced downstream. The vortex-breakdown efficiency of each configuration is systematically evaluated by measuring four KPIs: the pressure drop, the TKE reduction, the velocity uniformity, and the transmitted vortex size.

The size of the grid wires plays a key role. The bigger the wires are, the more distorted the transmitted vortex will be. Larger wires also create bigger wakes which extend further downstream, increasing the effects of subsequent grids. The wire diameter is a key design lever. Increasing the wire size increases the breakdown of the vortical structures, but creates a large wake that results in relatively high TKE levels. Smaller wires are less effective at breaking down vortical structures, but are better at reducing the residual TKE. The influence of placing multiple grids in series varies significantly with the wire diameter of the grids. When the wire diameter is small, the wake produced by the grids is relatively short and does not interact with the grids downstream unless they are extremely close.

For a given TKE reduction target, it is more efficient to reduce the wire diameter of the grids while keeping the porosity high. The same TKE reduction can be achieved for a much lower penalty in terms of the pressure drop. The pressure drop increases systematically when additional grids are introduced. However, the effect of the spacing between the grids depends on the grid alignment. When the grids are perfectly aligned, the wake generated by the upstream grids creates a low-pressure zone. The closer the next grids are, the more they can benefit from this drafting effect, resulting in a lower pressure drop. However, if

the grids are misaligned, increasing the distance between the grids is favorable to minimize the pressure drop. Finally, decreasing the porosity and the wire size result in higher flow uniformity due to the lower turbulence.

In conclusion, the optimal design should be a graded structure, starting with a very porous grid made from a large wire diameter to break down the incoming vortices. Additional grids should be rotated and offset to increase the tortuosity, as it improves the velocity homogeneity. The spacing between the grids should be as large as possible and their numbers must be kept to a minimum to avoid excessive pressure losses. The wire diameter of the final grid depends on the targeted TKE, and should be small if the TKE is nefarious, but should remain large if TKE is beneficial to the application. The porosity should only be reduced when the desired velocity uniformity is a concern.

The optimal grid diameter most probably varies with respect to the size of the incident vortices (and, by extension, the bluff body diameter which controls it). The authors would not want to portray the results as being universal. In future work, varying the size of the bluff body would provide valuable information to better understand how the ratio between the vortex size and wire diameter impacts the grid performance. It would also be valuable to rerun the models at higher Reynolds numbers to extend the results over a more meaningful range of conditions.

Author Contributions: Conceptualization, J.S. and V.B.; methodology, J.S. and M.S.; validation, J.S.; numerical analysis and post-processing, J.S.; writing—original draft preparation, J.S.; writing—review, M.S. and V.B.; supervision, M.S. and V.B.; project administration, V.B.; funding acquisition, F.S. All authors have read and agreed to the published version of the manuscript.

Funding: This research was funded by Siemens Energy Canada Limited.

Data Availability Statement: Data are contained within the article.

Acknowledgments: This research was enabled in part by support from Calcul Québec (www.calculquebec.ca) and the Digital Research Alliance of Canada (alliancecan.ca).

Conflicts of Interest: Authors Julien Sirois and Fabian Sanchez, were employed by the company Siemens Energy Canada Limited. The remaining authors declare that the research was conducted in the absence of any commercial or financial relationships that could be construed as a potential conflict of interest.

Nomenclature

TKE	Turbulent Kinetic Energy (J/kg)
ΔP	Pressure drop (Pa)
θ	Velocity Field Uniformity (%)
TVS	Transmitted Vortex Size (mm)
D	Diameter of the tunnel (mm)
d	Diameter of the bluff body (mm)
d_w	Diameter of the grid wires (mm)
ε	Inter-grid spacing (gap between two grids) (mm)
φ	Grid porosity (%)
ρ	Density (kg/m^3)
μ	Dynamic Viscosity (Pa·s)
U	Velocity (m/s)
F_D	Drag Force (N)
$A_{Frontal}$	Frontal Area (m^2)
Re_{BB}	Reynolds number based on bluff body diameter (-)
Re_{Pipe}	Reynolds number based on tunnel diameter (-)
St	Strouhal Number (-)

Appendix A

The shedding frequency of the vortices is function of the bluff body diameter and the flow velocity. It is calculated by measuring the period of the lift force fluctuations acting on the bluff body. The shedding frequency (f) is often expressed in terms of the Strouhal number (St). Based on empirical evidence in the literature, the Strouhal number for a cylindrical bluff body in the 49 > Re > 5000 range is around 0.20 ± 0.01 (Oliveira, Moraes [17]). It is calculated by Equation (A1), where f is the frequency, D_{BB} is the bluff body diameter, u is the velocity, ρ is the density, and μ is the dynamic viscosity.

$$St = \frac{f \cdot d}{U} \tag{A1}$$

The global target size and global refinement zone are kept constant at 2.5 and 1.0 mm, respectively. The mesh was first refined for the baseline condition, i.e., just the bluff body without the grids. The bluff body and its wake were refined successively until the drag coefficient stabilized to less than 1%, relative to the ultra-fine case. The intermediate mesh (#3) was selected because the drag coefficient (C_D) and St were within the typical range based on the literature [18,19]. The drag coefficient is calculated by Equation (A2), where F_D is the drag force acting on the bluff body. Note that the bluff body diameter (d) and the tunnel diameter (D) are in meters.

$$C_D = \frac{F_D}{\frac{1}{2} d \cdot D \cdot \rho \cdot U^2} \tag{A2}$$

Once the mesh for the baseline condition was satisfactory, a grid was introduced in the model. Again, the surface mesh and the wake of the grid were successively refined until the drag, on the grid this time, leveled to around 1% of the ultra-fine mesh. The configuration with the smallest wire and highest porosity (D025P85) was selected. The mesh size was kept constant for the other grids, regardless of the wire size.

Table A1. Mesh refinement table.

#	Cell Count	Cd	*St*	Cell Size [mm]	
				Surface	Wake
1	287,666	1.236	0.207	0.500	0.5
2	639,365	1.108	0.208	0.100	0.5
3	1,682,121	1.059	0.215	0.050	0.5
4	5,256,270	1.100	0.216	0.025	0.5

References

1. Lefebvre, A.H.; Ballal, D.R. *Gas Turbine Combustion*; CRC Press: Boca Raton, FL, USA, 2010; p. 560.
2. Hrynuk, J.T.; Stutz, C.M.; Bohl, D.G. Experimental Measurement of Vortex Ring Screen Interaction Using Flow Visualization and Molecular Tagging Velocimetry. *J. Fluids Eng.* **2018**, *140*, 111401. [CrossRef]
3. Hrynuk, J.T.; Van Luipen, J.; Bohl, D. Flow visualization of a vortex ring interaction with porous surfaces. *Phys. Fluids* **2012**, *24*, 037103. [CrossRef]
4. Musta, M.N.; Krueger, P.S. Interaction of vortex rings with multiple permeable screens. *Phys. Fluids* **2014**, *26*, 113101. [CrossRef]
5. Musta, M.N.; Krueger, P.S. Interaction of steady jets with an array of permeable screens. *Exp. Fluids* **2015**, *56*, 61. [CrossRef]
6. Naaktgeboren, C.; Krueger, P.S.; Lage, J.L. Interaction of a laminar vortex ring with a thin permeable screen. *J. Fluid Mech.* **2012**, *707*, 260–286. [CrossRef]
7. An, X.; Fultz, H.; Hassanipour, F. Experimental Study of Air Vortex Interaction with Porous Screens. *Spec. Top. Rev. Porous Media Int. J.* **2014**, *5*, 297–309. [CrossRef]
8. An, X.; Jiang, L.; Hassanipour, F. Numerical Analysis of Air Vortex Interaction with Porous Screen. *Fluids* **2021**, *6*, 70. [CrossRef]
9. Cheng, M.; Lou, J.; Lim, T.T. A numerical study of a vortex ring impacting a permeable wall. *Phys. Fluids* **2014**, *26*, 103602. [CrossRef]

10. Teruna, C.; Ragni, D.; Avallone, F.; Casalino, D. A rod-linear cascade model for emulating rotor-stator interaction noise in turbofans: A numerical study. *Aerosp. Sci. Technol.* **2019**, *90*, 275–288. [CrossRef]
11. Jacob, M.C.; Boudet, J.; Casalino, D.; Michard, M. A rod-airfoil experiment as a benchmark for broadband noise modeling. *Theor. Comput. Fluid Dyn.* **2005**, *19*, 171–196. [CrossRef]
12. Nguyen, Q.D.; Lu, W.; Chan, L.; Ooi, A.; Lei, C. A state-of-the-art review of flows past confined circular cylinders. *Phys. Fluids* **2023**, *35*, 071301. [CrossRef]
13. Durbin, P.A.; Speziale, C.G. Realizability of second-moment closure via stochastic analysis. *J. Fluid Mech.* **1994**, *280*, 395–407. [CrossRef]
14. Frank White, J.M. *Viscous Fluid Flow*, 4th ed.; McGraw Hill: New York, NY, USA, 2022.
15. Weltens, H.; Bressler, H.; Terres, F.; Neumaier, H.; Rammoser, D. *Optimisation of Catalytic Converter Gas Flow Distribution by CFD Prediction*; SAE International: Warrendale, PA, USA, 1993.
16. Ong, L.; Wallace, J. The velocity field of the turbulent very near wake of a circular cylinder. *Exp. Fluids* **1996**, *20*, 441–453. [CrossRef]
17. Oliveira, M.A.D.; Moraes, P.G.D.; Andrade, C.L.D.; Bimbato, A.M.; Alcântara Pereira, L.A. Control and Suppression of Vortex Shedding from a Slightly Rough Circular Cylinder by a Discrete Vortex Method. *Energies* **2020**, *13*, 4481. [CrossRef]
18. Norberg, C. Fluctuating lift on a circular cylinder: Review and new measurements. *J. Fluids Struct.* **2003**, *17*, 57–96. [CrossRef]
19. Heddleson, C.F.; Brown, D.L.; Cliffe, R.T. *Summary of Drag Coefficients of Various Shaped Cylinders*; General Electric Atomic Products Division: Cincinnati, OH, USA, 1957.